

Received 9 January 2024; revised 14 February 2024 and 2 March 2024; accepted 13 March 2024. Date of publication 20 March 2024;  
date of current version 4 April 2024. The review of this paper was arranged by Associate Editor Lingxiao Xue.

Digital Object Identifier 10.1109/OJPEL2024.3379846

# 50 kW Reflexive Tuning Networks With Low Uncoupled Transmitter Currents for Dynamic Inductive Power Transfer Systems

**SHUNTARO INOUE<sup>1</sup>** (Member, IEEE), **SAMUEL KIGUTHI<sup>1</sup>**, **JONATHAN NEWMAN<sup>1</sup>**, **TIMOTHY GOODALE<sup>1</sup>**,  
**CHAKRIDHAR REDDY TEENETI<sup>1</sup>** (Member, IEEE), **BRYCE HESTERMAN<sup>1</sup>** (Life Member, IEEE),  
**ABHILASH KAMINENI<sup>1</sup>** (Member, IEEE), AND **REGAN ANDREW ZANE<sup>1</sup>** (Senior Member, IEEE)

<sup>1</sup>Department of Electrical and Computer Engineering, Utah State University, Logan, UT 84341 USA

<sup>2</sup>ASPIRE, Logan, UT 84341 USA

CORRESPONDING AUTHOR: SHUNTARO INOUE (e-mail: shuntaro0628@gmail.com)

This work was supported in part by the Advancing Sustainability through Powered Infrastructure for Roadway Electrification Center (ASPIRE), an NSF ERC, under Grant 1941524, and in part by Toyota Central R&D Laboratories, Inc.

**ABSTRACT** This paper proposes a novel reflexive tuning dynamic inductive power transfer (DIPT) system with a single inverter connected to multiple transmitter coils, which makes DIPT systems simpler and more cost-effective. Traditional DIPT systems have an individual inverter per transmitter coil, leading to considerable costs when transmitter coils span long distances on roads. The proposed reflexive tuning DIPT system leverages a reflected reactance from a receiver coil to allow a single inverter to drive multiple transmitter coils. Using reflexive tuning, the approach naturally achieves high currents solely on the transmitter coil coupled with a receiver coil when a vehicle moves along a DIPT roadway. Simultaneously, the other uncoupled transmitter coils connected to the shared inverter operate at notably reduced currents. Theoretical analysis, design, simulation, and experimental results are provided for the proposed reflexive tuning circuits. Simulation results indicate that the proposed reflexive tuning circuit can reduce the uncoupled transmitter current by 37% compared to the conventional double-sided LCC tuning circuit while maintaining the output power at the same level. Experimental results with a 50 kW prototype demonstrate operation on both automated rail and vehicle systems. The results demonstrate dc-dc efficiency of 90% per a single transmitter coil configuration with 223 mm air gap and capability of power delivery at least up to 60 km/h speed.

**INDEX TERMS** Dynamic inductive power transfer, inductive power transfer, reflexive tuning, double-sided LCC tuning.

## I. INTRODUCTION

Electric vehicles (EVs) are increasingly gathering interest due to their zero tailpipe emissions and lower running costs. However, EVs suffer from a limited driving range, longer charging time, and higher upfront costs. Dynamic inductive power transfer (DIPT) offers a promising solution to these issues by enabling EVs to cover more distance with a smaller battery pack [1], [2]. Thereby, DIPT has the potential to make EVs more affordable and increase their adoption in the market.

DIPT systems include many components such as inverters, transmitter coils, receiver coils, rectifiers, and resonant capac-

itors [3], [4], [5], [6], [7], [8], [9], [10], [11], [12], [13], [14], [15]. System characteristics, such as cost, efficiency, and stray magnetic fields vary depending on the system configurations. Therefore, over the decades, several types of DIPT systems have been studied and they have tradeoffs.

DIPT systems can be divided into two major categories based on the coil configuration: long-track transmitters and short-individual transmitters [16], [17], [18], [19], [20]. The long-track transmitter has transmitter coils that are significantly larger than the receiver coils. Its advantage is simplicity and a minimal number of inverters and compensation networks [21], [22], [23], [24], [25], [26], [27], [28]. However,

it has several drawbacks. First, the coil generates a stray magnetic field in a large area since a long stretch of road has a coil that is excited with high current, even while a receiver coil only covers a small portion of the transmitter, resulting in difficulty maintaining stray fields below the safety limits [26], [27], [28]. Secondly, the long track design has a higher self-inductance due to the longer coil length, which creates high voltages across the coil terminals. Third, the coupling coefficient becomes quite low due to the large uncoupled area of the transmitter coil, resulting in low system efficiency.

In the short-individual transmitter configuration, the transmitter size is close to the receiver size, and each transmitter coil has its own inverter and compensation network [29], [30], [31], [32]. This configuration allows for selective excitation of each transmitter coil as it becomes aligned with a receiver coil, resulting in high system efficiency and well-maintained stray magnetic fields. The drawback of the short-individual transmitter configuration is its complexity since it requires a large number of inverters and compensation components. The cost for the system turns out quite expensive compared to the long-track transmitter configuration [29].

Additionally, hybrid solutions have been considered that use short transmitter coils but share aspects of the compensation components and inverter circuitry to reduce cost compared to the short-individual configuration or to improve efficiency and stray fields compared to the long-track configuration. A parallel-connected double-sided LCC setup was proposed in [33] to reduce the number of inverters. This arrangement connects six transmitter coils and their compensation networks in parallel, powered by a single inverter. By utilizing the double-sided LCC's characteristic, the shared inverter's current caused by the uncoupled transmitter coils is close to zero, resulting in minimizing extra inverter loss. However, this configuration has a drawback: it results in high uncoupled transmitter currents. The constant transmitter current characteristic of the double-sided LCC tuning network increases overall system losses and stray magnetic fields when compared to the short-individual transmitter configuration.

In order to reduce the uncoupled transmitter current, a reflexive tuning method was proposed in [34]. It switches resonated transmitter coils utilizing reflected reactance from the receiver coil and can reduce the uncoupled transmitter current compared to the parallel connected double-sided LCC configuration, as shown in Fig. 1. The system has parallel connected transmitter coils and compensation networks, powered by a single inverter. A reflected reactance created in the transmitter coils varies according to the position of the receiver coil. When a transmitter coil aligns with a receiver coil, the system is designed to resonate and generate strong magnetic fields, allowing power transfer. Consequently, the system is capable of automatically adjusting the transmitter current amplitude, resulting in low stray magnetic fields and loss from the uncoupled transmitter coils, delivering wireless power from the coupled transmitter coil.

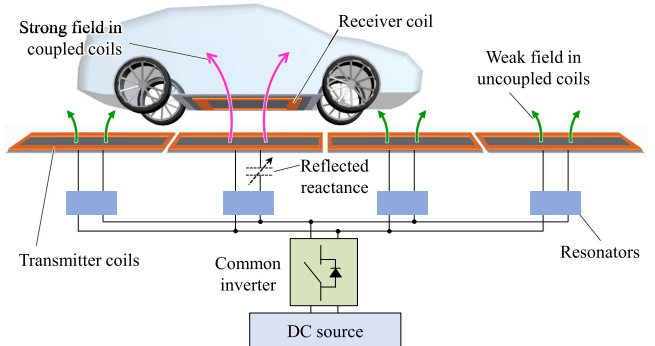


**FIGURE 1.** The conceptual diagram of the reflexive tuning.

In the previous study [34], a 300 W prototype was demonstrated using an output resistive load through the static power transfer condition at multiple positions. However, the conventional reflexive tuning circuit struggles to maintain the low uncoupled transmitter current with high output power designs. The issue emerges because the conventional reflexive tuning circuit's output power and uncoupled transmitter current rely on a singular design parameter: the capacitance ratio within the compensation network.

To overcome the issue, this paper proposes a novel reflexive tuning circuit with extra design parameters, enabling the designs with further reduced uncoupled transmitter currents. Additionally, soft switching analysis and output power characteristics for input and output voltages are provided and dynamic wireless power transfer tests are conducted in order to facilitate high power dynamic wireless power transfer operation with the proposed solution.

The contributions of this paper are as follows: First, the paper proposes a new reflexive tuning circuit to achieve low uncoupled transmitter currents. Second, the theoretical soft switching region is analyzed and verified in simulation. Third, the theoretical output power characteristics with input and output voltages are analyzed. Fourth, a 50 kW prototype is constructed and dynamic power transfer characteristics of the reflexive tuning circuit are evaluated.

The analyses, design, and test are organized into four sections. Section II starts with a comparison of the configuration between the conventional and proposed reflexive tuning circuits. In Section III, theoretical analyses of the proposed circuit including the soft switching analysis are presented. In Section IV, the proposed circuit is designed with 50 kW output power, and the output power characteristics are analyzed. In Section V, the designed circuit is prototyped and tested on an automated rail and a vehicle for dynamic power transfer tests.

## II. PROPOSED REFLEXIVE TUNING TOPOLOGY

The conventional reflexive tuning circuit topology [34] is shown in Fig. 2. Each compensation network on the transmitter side has a parallel compensation capacitor  $C_{i,p}$  ( $i = 1, \dots, n$ ) and a series compensation capacitor  $C_{i,s}$ . On the

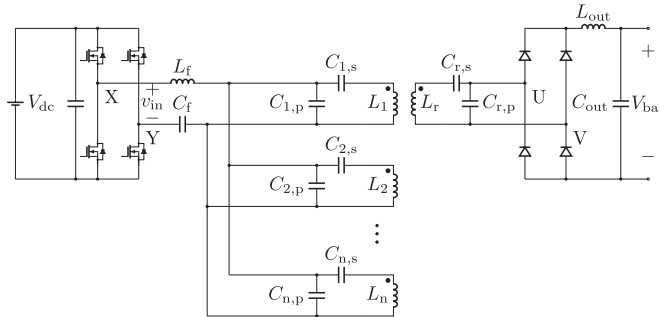


FIGURE 2. Conventional reflexive tuning circuit [34].

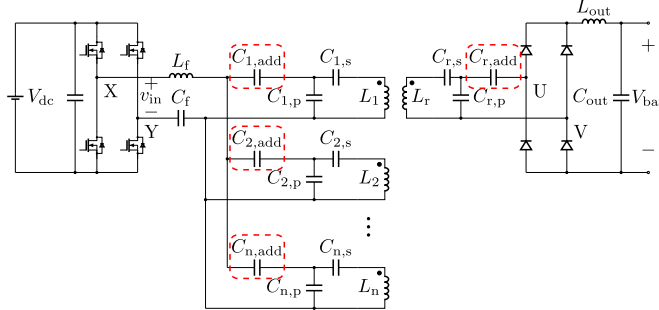


FIGURE 3. Proposed reflexive tuning circuit.

receiver side, a series compensation capacitor  $C_{r,s}$  and a parallel compensation capacitor  $C_{r,p}$  are attached. Additionally, it consists of a bandpass filter formed by  $L_f$  and  $C_f$  on the inverter side. The purpose of the bandpass filter is to reduce switching loss due to harmonics in the inverter current from the uncoupled transmitter coils.  $L_f$  and  $C_f$  are defined by

$$f_{sw} = \frac{1}{2\pi\sqrt{L_f C_f}}. \quad (1)$$

where  $f_{sw}$  is the switching frequency of the inverter.

The conventional reflexive tuning circuit requires an output inductor  $L_{out}$  between the secondary compensation circuit and the output voltage  $V_{bat}$  since  $C_{r,p}$  can be assumed as a voltage source, and switching action of the diode rectifier creates large current spikes if  $L_{out}$  is not attached between  $C_{r,p}$  and  $V_{bat}$ .

The proposed reflexive tuning circuit is shown in Fig. 3. Compared to the conventional reflexive tuning circuit, the proposed circuit has additional series capacitors  $C_{i,\text{add}}$  and  $C_{r,\text{add}}$  on the transmitter and receiver side, respectively. The transmitter side capacitor  $C_{i,\text{add}}$  works as a voltage divider and can reduce the applied voltage to the uncoupled transmitter coils, reducing the uncoupled transmitter currents. The capacitor  $C_{r,\text{add}}$  on the receiver side can amplify the reflected reactance in a transmitter coil, leading to an increase in the variation of the transmitter current amplitude.

The proposed circuit introduces greater design flexibility due to the added series compensation capacitors on both the transmitter and receiver sides. This enhanced reflexive tuning

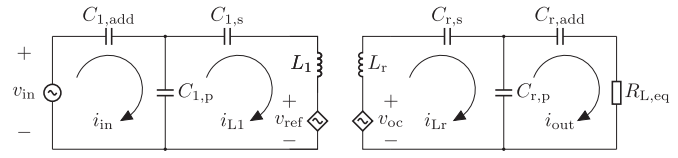


FIGURE 4. Equivalent circuit of the proposed reflexive tuning network.

topology allows for designs with reduced uncoupled transmitter currents while maintaining output power at the same level compared to the conventional reflexive tuning circuit.

### III. THEORETICAL ANALYSIS OF THE PROPOSED CIRCUIT

Theoretical equations to design the proposed circuit are derived in this section.

#### A. OUTPUT POWER

For simplicity, only the first transmitter coil ( $i = 1$ ) is considered in this analysis. The equivalent circuit of the proposed reflexive tuning network is shown in Fig. 4. Circuit equations can be written in a matrix form as

$$\begin{bmatrix} \frac{C_{1,\text{add}}+C_{1,p}}{j\omega C_{1,\text{add}}C_{1,p}} & -\frac{1}{j\omega C_{1,p}} \\ -\frac{1}{j\omega C_{1,p}} & j\omega L_1 + \frac{C_{1,s}+C_{1,p}}{j\omega C_{1,p}C_{1,s}} \end{bmatrix} \cdot \begin{bmatrix} i_{in} \\ i_{L1} \end{bmatrix} = \begin{bmatrix} v_{in} \\ -v_{ref} \end{bmatrix} \quad (2)$$

$$\begin{bmatrix} j\omega L_r + \frac{C_{r,s}+C_{r,p}}{j\omega C_{r,s}C_{r,p}} & -\frac{1}{j\omega C_{r,p}} \\ -\frac{1}{j\omega C_{r,p}} & \frac{C_{r,\text{add}}+C_{r,p}}{j\omega C_{r,\text{add}}C_{r,p}} + R_{L,\text{eq}} \end{bmatrix} \cdot \begin{bmatrix} i_{Lr} \\ i_{out} \end{bmatrix} = \begin{bmatrix} v_{oc} \\ 0 \end{bmatrix} \quad (3)$$

where  $\omega$  is the angular switching frequency of the inverter,  $v_{in}$  is the inverter voltage,  $v_{ref}$  is the reflected voltage at the transmitter coil,  $v_{oc}$  is the induced voltage at the receiver coil,  $R_{L,\text{eq}}$  is the equivalent load resistance, and  $k_{1,r}$  is the coupling coefficient between the transmitter coil  $L_1$  and the receiver coil  $L_r$ .

From Fourier transform, the rectangular shaped inverter voltage  $v_{in}$  is represented as

$$v_{in} = \frac{4V_{dc}}{\pi} \sum_{m=1,3,5,\dots}^{\infty} \frac{1}{m} e^{j\omega t} \quad (4)$$

$$\simeq \frac{4V_{dc}}{\pi} e^{j\omega t}. \quad (5)$$

The reflected voltage  $v_{ref}$  and the induced voltage  $v_{oc}$  are represented as

$$v_{ref} = -j\omega k_{1,r} \sqrt{L_1 L_r} i_{L1}, \quad (6)$$

$$v_{oc} = j\omega k_{1,r} \sqrt{L_1 L_r} i_{Lr}. \quad (7)$$

The induced voltage  $v_{oc}$  is equivalent to the measured voltage when the receiver coil is set as an open circuit with the transmitter current  $i_{L1}$ .

In the uncoupled condition ( $k_{1,r} = 0$ ), the transmitter side's resonant equation is represented as

$$j\omega L_1 + \frac{1}{j\omega C_{1,s}} + \frac{1}{j\omega C_{1,p}} = 0. \quad (8)$$

In the fully coupled condition ( $k_{1,r} = k_{\lim}$ ), the transmitter side's resonant equation is written as

$$\frac{1}{j\omega(C_{1,p} + C_{1,\text{add}})} + \frac{1}{j\omega C_{1,s}} + j\omega L_1 - jX_{\text{ref}}|_{k_{1,r}=k_{\lim}} = 0. \quad (9)$$

where  $X_{\text{ref}}$  represents reflected reactance. The receiver side's resonant equation is represented as

$$\frac{1}{j\omega C_{r,s}} + \frac{1}{j\omega C_{r,p}} + j\omega L_r = 0. \quad (10)$$

From (3) and (10), the receiver coil current  $i_{Lr}$  is represented as

$$i_{Lr} = \left(1 + \frac{C_{r,p}}{C_{r,\text{add}}} + j\omega C_{r,p} R_{L,\text{eq}}\right) \omega^2 C_{r,p} k_{1,r} \sqrt{L_1 L_r} i_{L1}. \quad (11)$$

Therefore, using (6) and (11), the reflected impedance  $Z_{\text{ref}}$  is represented as

$$Z_{\text{ref}} = \frac{v_{\text{ref}}}{i_{L1}} \quad (12)$$

$$= \frac{c_2^2 k_{1,r}^2 L_1}{L_r} R_{L,\text{eq}} - j\omega c_2 c_3 k_{1,r}^2 L_1. \quad (13)$$

where

$$c_2 = 1 + \frac{C_{r,p}}{C_{r,s}}, \quad c_3 = 1 + \frac{C_{r,p}}{C_{r,\text{add}}}. \quad (14)$$

Since the reflected impedance  $Z_{\text{ref}}$  is represented as

$$Z_{\text{ref}} = R_{\text{ref}} - jX_{\text{ref}}, \quad (15)$$

the reflected resistance  $R_{\text{ref}}$  and reflected reactance  $X_{\text{ref}}$  are solved by comparing between (13) and (15), and represented as

$$R_{\text{ref}} = \frac{c_2^2 k_{1,r}^2 L_1}{L_r} R_{L,\text{eq}}, \quad (16)$$

$$X_{\text{ref}} = \omega c_2 c_3 k_{1,r}^2 L_1. \quad (17)$$

From (8), (9), and (17),  $C_{1,p}$  is derived as

$$C_{1,p} = \frac{1}{\omega^2 c_1 c_2 c_3 k_{\lim}^2 L_1}. \quad (18)$$

where

$$c_1 = 1 + \frac{C_{1,p}}{C_{1,\text{add}}}. \quad (19)$$

From (8) and (18),

$$C_{1,s} = \frac{1}{\omega^2 L_1 (1 - c_1 c_2 c_3 k_{\lim}^2)}. \quad (20)$$

From (18) and (19),

$$C_{1,\text{add}} = \frac{C_{1,p}}{c_1 - 1} = \frac{1}{\omega^2 c_1 (c_1 - 1) c_2 c_3 k_{\lim}^2 L_1}. \quad (21)$$

From (10) and (14), the compensation components on the receiver side  $C_{r,s}$ ,  $C_{r,p}$ ,  $C_{r,\text{add}}$  are represented by

$$C_{r,s} = \frac{c_2}{\omega^2 (c_2 - 1) L_r}, \quad (22)$$

$$C_{r,p} = \frac{c_2}{\omega^2 L_r}, \quad (23)$$

$$C_{r,\text{add}} = \frac{c_2}{\omega^2 (c_3 - 1) L_r}. \quad (24)$$

By solving (2) and (3) using the derived equations of compensation capacitors, the transmitter current  $i_{L1}$  and output current  $i_{\text{out}}$  are represented as

$$i_{L1} = \frac{L_r v_{\text{in}}}{c_1 c_2 L_1 \left\{ c_2 k_{1,r}^2 R_{L,\text{eq}} + j\omega c_3 (k_{\lim}^2 - k_{1,r}^2) L_r \right\}}, \quad (25)$$

$$i_{\text{out}} = \frac{k_{1,r} \sqrt{L_r} v_{\text{in}}}{c_1 \sqrt{L_1} \left\{ c_2 k_{1,r}^2 R_{L,\text{eq}} + j\omega c_3 (k_{\lim}^2 - k_{1,r}^2) L_r \right\}}. \quad (26)$$

From (25), the transmitter current in the uncoupled condition ( $k_{1,r} = 0$ ) is represented as

$$i_{L1}|_{k_{1,r}=0} = \frac{v_{\text{in}}}{j\omega c_1 c_2 c_3 k_{\lim}^2 L_1}, \quad (27)$$

From (26), the output power  $P_{\text{out}}$  can be calculated as

$$P_{\text{out}} = R_{L,\text{eq}} \left( \frac{i_{\text{out}}}{\sqrt{2}} \right)^2 \quad (28)$$

$$= R_{L,\text{eq}} c_2^2 k_{1,r}^2 \frac{L_1}{L_r} \left( \frac{i_{L1}}{\sqrt{2}} \right)^2 \quad (29)$$

$$= \frac{8 k_{1,r}^2 L_r R_{L,\text{eq}} V_{dc}^2}{\pi^2 c_1^2 L_1 \left\{ c_2^2 k_{1,r}^4 R_{L,\text{eq}}^2 + \omega^2 c_3^2 (k_{\lim}^2 - k_{1,r}^2)^2 L_r^2 \right\}}. \quad (30)$$

$R_{L,\text{eq}}$  is derived by solving the following equation as

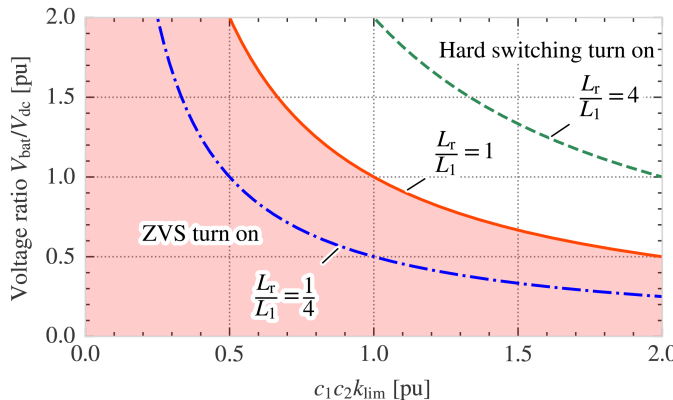
$$\left| i_{\text{out}} \right| \cdot R_{L,\text{eq}} = \frac{4V_{bat}}{\pi} \quad (31)$$

$$\Leftrightarrow R_{L,\text{eq}} = \frac{\omega c_1 c_3 (k_{\lim}^2 - k_{1,r}^2) \sqrt{L_1 L_r}}{k_{1,r} \sqrt{\left| L_r \left( \frac{V_{dc}}{V_{bat}} \right)^2 - c_1^2 c_2^2 k_{1,r}^2 L_1 \right|}}. \quad (32)$$

(19) It is noteworthy that  $R_{L,\text{eq}}$  is varied depending on the coupling condition  $k_{1,r}$ .

Using the (30) and (32), the output power  $P_{\text{out}}$  can be calculated for any coupling coefficient  $k_{1,r}$ . Notably, if parasitic resistances are ignored, the output power approaches infinity when  $k_{1,r} = k_{\lim}$ .

In accordance with the (29), it is evident that the output power  $P_{\text{out}}$  exhibits a quadratic proportionality to the transmitter current  $i_{L1}$ . Consequently, to achieve high power output during the coupling condition, it is necessary to apply

**FIGURE 5.** ZVS region.

a high transmitter current. Conversely, during the uncoupled condition, a low transmitter current is required to minimize undesirable losses and stray magnetic fields generated from the uncoupled transmitter coils. Therefore, a high coupled transmitter current and a low uncoupled transmitter current are desired for the reflexive tuning circuits.

### B. SOFT SWITCHING ANALYSIS

This section investigates the zero-voltage-switching (ZVS) region when the inverter's transistors turn on. The inverter current  $i_{\text{in}}$  is represented as

$$i_{\text{in}} = \frac{k_{1,\text{r}}^2 (\omega c_3 L_{\text{r}} + j c_2 R_{L,\text{eq}}) v_{\text{in}}}{\omega c_1^2 c_2 c_3 k_{\text{lim}}^2 L_1 \left\{ c_2 k_{1,\text{r}}^2 R_{L,\text{eq}} + j \omega c_3 (k_{\text{lim}}^2 - k_{1,\text{r}}^2) L_{\text{r}} \right\}}. \quad (33)$$

If the imaginary part of inverter current  $i_{\text{in}}$  is negative, the inverter's transistors achieve ZVS. Hence, the ZVS requirements can be written using (32) and (33) as

$$\text{Im}(i_{\text{in}}) < 0 \quad (34)$$

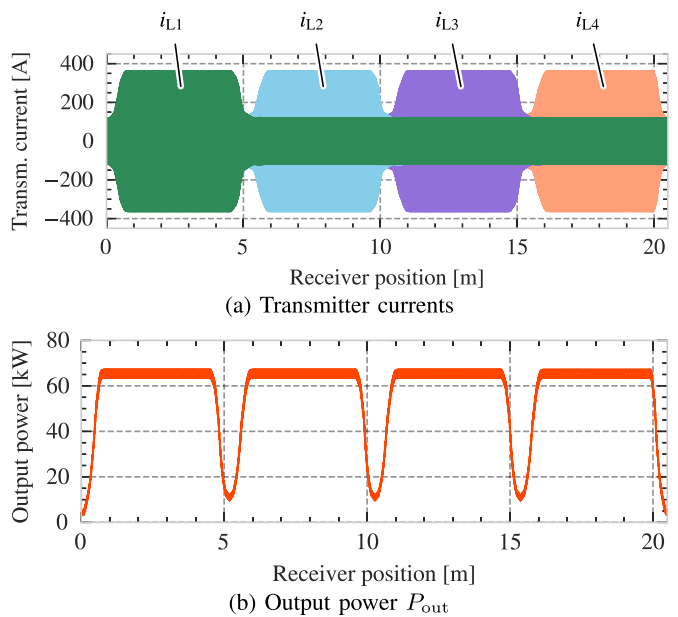
$$\Leftrightarrow (c_2 k_{1,\text{r}})^2 R_{L,\text{eq}} < (k_{\text{lim}}^2 - k_{1,\text{r}}^2) (\omega c_3 L_{\text{r}})^2 \quad (35)$$

$$\Leftrightarrow \frac{V_{\text{bat}}}{V_{\text{dc}}} < \frac{1}{c_1 c_2 k_{\text{lim}}} \sqrt{\frac{L_{\text{r}}}{L_1}}. \quad (36)$$

where

$$k_{1,\text{r}} < \frac{1}{c_1 c_2} \frac{V_{\text{dc}}}{V_{\text{bat}}} \sqrt{\frac{L_{\text{r}}}{L_1}}. \quad (37)$$

The ZVS condition, as described in (36), remains sustainable as long as the coupling coefficient  $k_{1,\text{r}}$  adheres to the condition (37). Importantly, it's worth noting that the ZVS condition remains unaffected by the value of the coupling coefficient  $k_{1,\text{r}}$ . The ZVS boundary is depicted on the surface of the voltage ratio  $V_{\text{bat}}/V_{\text{dc}}$  and the multiplication of design parameters  $c_1 c_2 k_{\text{lim}}$  when the ratio of self-inductance  $L_{\text{r}}/L_1$  is varied in three patterns, as shown in Fig. 5. The solid red line shows the ZVS boundary when  $L_{\text{r}}/L_1 = 1$ , and the area below the

**FIGURE 6.** Conceptual operational waveforms of the proposed reflexive tuning circuit.

boundary is the ZVS region. As the ratio of self-inductance  $L_{\text{r}}/L_1$  increases, the ZVS region is enlarged.

### C. COMPARISON OF PROPOSED AND CONVENTIONAL REFLEXIVE TUNING CIRCUITS

A comprehensive comparison between the proposed and conventional reflexive tuning circuits is presented in Table 1. The theoretical equation for the uncoupled transmitter current  $|i_{L1}|_{k_{1,\text{r}}=0}$  and output power  $P_{\text{out}}$  of the conventional reflexive tuning circuit is derived by specifically setting  $c_1 = 1$  and  $c_3 = 1$  in the equations formulated for the proposed circuit presented in equations (27) and (30). One noteworthy outcome of this comparative analysis is that when both circuits are engineered to deliver identical output power levels, the proposed circuit consistently demonstrates the ability to achieve lower uncoupled transmitter currents. This advantage is attributed to the flexibility provided by the design parameters  $c_1$  and  $c_3$ , which the conventional circuit lacks.

### D. CONCEPTUAL OPERATIONAL WAVEFORMS OF THE PROPOSED REFLEXIVE TUNING CIRCUIT

An example of operational waveforms of the proposed circuit is shown in Fig. 6. Four transmitter coils with the proposed reflexive tuning circuit are set on the ground and a receiver coil moves above the transmitter coils. The lengths of the transmitter and receiver coils along the vehicle motion direction are 5 m and 0.85 m, respectively.

Fig. 6(a) depicts the transmitter current waveforms in relation to the position of the receiver coil. Notably, the amplitude of each transmitter current increases when the receiver coil aligns with each respective transmitter coil, and other uncoupled transmitter currents are kept low. This characteristic

**TABLE 1.** Comprehensive Comparison Between the Proposed and Conventional Reflexive Tuning Circuits

	Conventional reflexive	Proposed reflexive
Uncoupled	<p>Inverter current <math>i_{in} = 0</math></p>	<p>Inverter current <math>i_{in} = 0</math></p> <p><math>c_1 = \frac{C_{1,p}}{C_{1,add}} + 1</math></p>
Coupled	<p><math>c_2 = \frac{C_{r,p}}{C_{r,s}} + 1</math></p>	<p><math>c_2 = \frac{C_{r,p}}{C_{r,s}} + 1</math></p> <p><math>c_3 = \frac{C_{r,p}}{C_{r,add}} + 1</math></p>
Output power	$P_{out} = \frac{8 k_{1,r}^2 L_r R_{L,eq} V_{dc}^2}{\pi^2 L_1 \{c_2^2 k_{1,r}^4 R_{L,eq}^2 + \omega^2 (k_{lim}^2 - k_{1,r}^2)^2 L_r^2\}}$ <p><b>Same</b></p>	$P_{out} = \frac{8 k_{1,r}^2 L_r R_{L,eq} V_{dc}^2}{\pi^2 c_1^2 L_1 \{c_2^2 k_{1,r}^4 R_{L,eq}^2 + \omega^2 c_3^2 (k_{lim}^2 - k_{1,r}^2)^2 L_r^2\}}$ <p><b>Same</b></p>
Uncoupled transmitter current	$i_{L1} \Big _{k_{1,r}=0} = \frac{v_{in}}{\omega c_2 k_{lim}^2 L_1} \propto \frac{1}{c_2}$ <p><b>High X</b></p>	$i_{L1} \Big _{k_{1,r}=0} = \frac{v_{in}}{\omega c_1 c_2 c_3 k_{lim}^2 L_1} \propto \frac{1}{c_1 c_2 c_3}$ <p><b>Low ✓</b></p>

contributes to keeping total transmitter coil loss low when a shared inverter is utilized.

In Fig. 6(b), the output power is illustrated in relation to the position of the receiver coil. When the receiver coil is positioned above the transmitter coil, the output power remains consistent due to the substantial length difference between the transmitter and receiver coils. The output power distribution exhibits dips when the receiver coil is positioned between the transmitter coils. However, these power dips have a limited impact on the average output power since the duration of the flat power period significantly exceeds that of the power dips.

The impact of the power dips increases when a shorter transmitter coil is utilized. However, in this paper, a short transmitter coil is utilized due to practical challenges associated with handling long transmitter coils throughout research activities. In addition to utilizing longer transmitter coils, there are studies focused on improving power dips by adding DC-DC converters [35], [36] and modifications to coil geometry such as the DDQ coil as proposed in [11]. In contrast, this research takes a more fundamental approach, emphasizing how to drive multiple coils with a single inverter in a simple configuration without the need for additional components. As this is a fundamental study, there is flexibility to incorporate additional power dip improvement strategies in the future.

#### IV. DESIGN AND SIMULATION

The proposed circuit is designed and simulated on a circuit simulator to verify the validity of the theoretical analysis.

##### A. 3D FEM MODEL

A finite element method (FEM) model to demonstrate the design of the proposed reflexive tuning circuit is shown in

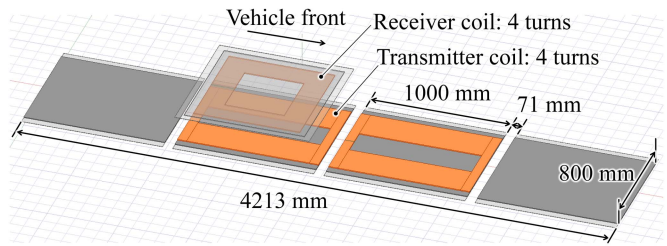


**FIGURE 7.** 3D FEM simulation model.

Fig. 7. Self-inductances  $L_1, L_r$  and coupling coefficient  $k_{1,r}$  are calculated to use the values in circuit designs. The transmitter and receiver coils have four turn windings, and the length and width of the transmitter coil are 1000 mm and 800 mm, respectively.

#### B. DESIGN OF THE PROPOSED REFLEXIVE, CONVENTIONAL REFLEXIVE, AND DOUBLE-SIDED LCC CIRCUITS

In the proposed reflexive tuning circuit, increasing  $c_1$  can reduce the uncoupled transmitter current, contributing to an improvement in system efficiency. However, there is a trade-off, as increasing  $c_1$  also results in a decrease in the output power. Increasing  $c_2$  enhances the reflected reactance, creating a significant difference between the uncoupled and coupled transmitter currents. This contributes to a reduction in the uncoupled transmitter current. A trade-off exists, as increasing  $c_2$  leads to a decrease in the output power. Similarly, increasing  $c_3$  raises the reflected reactance, which can reduce the current in the uncoupled transmitter coil, resulting in contributing to an improvement in system efficiency. However, a larger  $c_3$  results in an increase in the

**TABLE 2.** Shared Design Parameters Between the Proposed Reflexive, Conventional Reflexive, and Double-Sided LCC Circuits

Parameter	Symbol	Value	Unit
Input voltage	$V_{dc}$	400	V
Output voltage	$V_{bat}$	400	V
Air gap	$z_{gap}$	223	mm
Switching frequency	$f_{sw}$	85	kHz
Coupling coefficient between $L_1$ & $L_r$	$k_{1,r}$	0.00~0.22	-
Transmitter coil inductance	$L_1$	24.38	$\mu$ H
Receiver coil inductance	$L_r$	21.94	$\mu$ H
Filter inductor	$L_f$	5.31	$\mu$ H
Filter capacitor	$C_f$	0.66	$\mu$ F
Output dc inductor	$L_{dc}$	15.00	$\mu$ H
Number of turns of the transmitter coils	$N_{L1}$	4	turn
Number of turns of the receiver coil	$N_{Lr}$	4	turn

**TABLE 3.** Separated Design Parameters for the Proposed and Conventional Reflexive Tuning Circuits

Parameter	Symbol	Proposed	Conventional	Unit
Ratio of capacitors 1 + $C_{1,p}/C_{1,add}$	$c_1$	1.19	1.00	-
Ratio of capacitors 1 + $C_{r,p}/C_{r,s}$	$c_2$	3.10	3.10	-
Ratio of capacitors 1 + $C_{r,p}/C_{r,add}$	$c_3$	1.36	1.00	-
Added series capacitor	$C_{1,add}$	2.33	-	$\mu$ F
Series capacitor	$C_{1,s}$	212	192	nF
Parallel capacitor	$C_{1,p}$	446	568	nF
Added series capacitor	$C_{r,add}$	1.38	-	$\mu$ F
Series capacitor	$C_{r,s}$	235	235	nF
Parallel capacitor	$C_{r,p}$	494	495	nF
Limit of $k_{1,r}$	$k_{lim}$	0.253	0.285	-

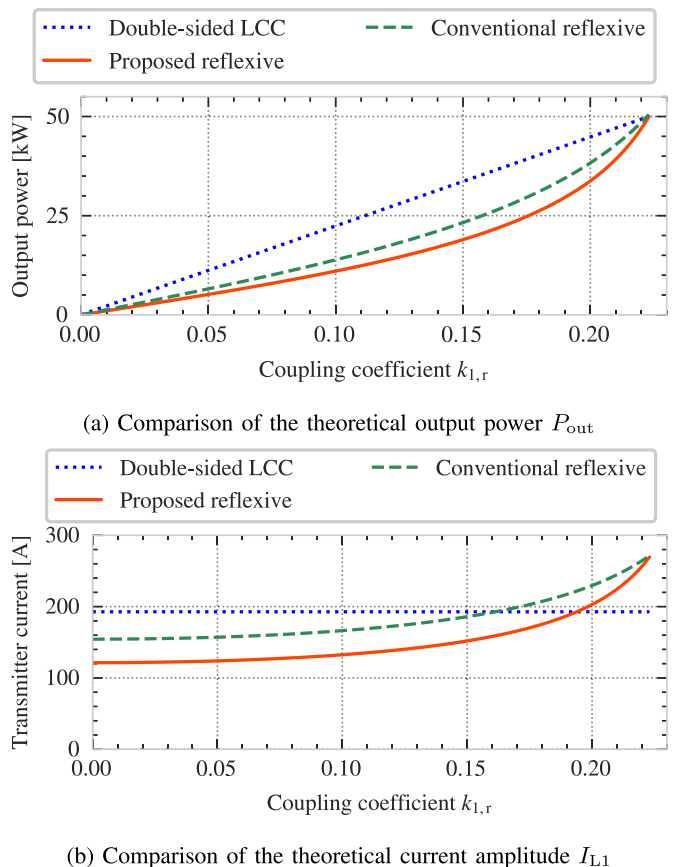
receiver coil current, resulting in increasing receiver coil loss. Therefore, it is necessary to design  $c_1$ ,  $c_2$ , and  $c_3$  in a way that optimizes system efficiency while meeting the output power requirements.

Shared design parameters between the proposed reflexive, conventional reflexive, and double-sided LCC circuits are listed in Table 2. The input voltage  $V_{dc}$  and output voltage  $V_{bat}$  are set to 400 V. The inverter's switching frequency is set to 85 kHz to follow the SAE standard [37]. The coupling coefficient between the transmitter and receiver coils  $k_{1,r}$  varies from 0 to 0.22, according to the position of the receiver coil due to longitudinal misalignment. This range of coupling coefficient  $k_{1,r}$  was extracted from the FEM simulations.

Separated designed parameters of the proposed and conventional reflexive tuning circuits are shown in Table 3. The circuits were designed to achieve an output power of 50 kW with a value of  $k_{1,r} = 0.22$ . For the conventional reflexive tuning circuit, design parameters  $c_1$  and  $c_3$  are assumed to be 1, as it lacks  $C_{1,add}$  and  $C_{r,add}$ . The double-sided LCC circuit was designed based on the optimization algorithm presented in [38].

### C. DESIGN RESULTS OF THE TRANSMITTER CURRENT AND OUTPUT POWER

Fig. 8 shows the sweep results of the theoretical output power and transmitter current amplitude  $I_{L1}$  (zero-to-peak) as the

**FIGURE 8.** Desing results of the transmitter current and output power.

coupling coefficient  $k_{1,r}$  varies from 0.00 to 0.22. The theoretical values for the double-sided LCC, conventional reflexive, and proposed reflexive circuits are represented by dotted, dashed, and solid lines, respectively.

The comparison of the output power  $P_{out}$  with respect to the coupling coefficient  $k_{1,r}$  is shown in Fig. 8(a). While the double-sided LCC circuit displays a linear relationship with  $k_{1,r}$ , both the proposed and conventional reflexive tuning circuits exhibit nonlinear characteristics. At the peak-coupled condition ( $k_{1,r} = 0.22$ ), all circuits are designed to deliver an output power of 50 kW.

In Fig. 8(b), a comparison of the transmitter current  $i_{L1}$  with respect to the coupling coefficient  $k_{1,r}$  is presented. Notably, the proposed circuit exhibits the lowest transmitter current in the uncoupled condition ( $k_{1,r} = 0$ ) among the three circuits. Specifically, the uncoupled transmitter current in the proposed reflexive tuning circuit measures 121.4 A (zero-to-peak), demonstrating a 21% reduction compared to the conventional reflexive tuning circuit and a 37% reduction compared to the double-sided LCC circuit.

### D. CIRCUIT SIMULATION FOR SOFT-SWITCHING ANALYSIS

Circuit simulations with different input and output voltage pairs are conducted to verify the soft-switching analysis

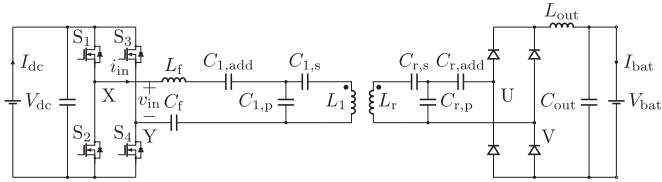


**FIGURE 9.** LTspice simulation model of the proposed circuit.

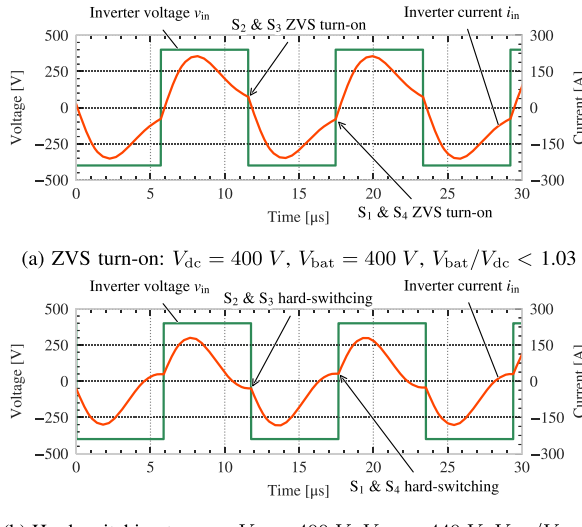


**FIGURE 10.** LTspice-simulated waveforms.

presented in the previous section. The circuit diagram and parameters used in the LTspice simulations are shown in Fig. 9, Tables 2, and 3.

The simulation results of the soft-switching analysis are shown in Fig. 10. The ZVS condition presented in (36) indicates that the voltage ratio  $V_{bat}/V_{dc}$  must be less than 1.03 to satisfy the ZVS requirement. The simulation waveforms demonstrate ZVS turn-on because the inverter current remains positive during the transition of the inverter voltage from positive to negative.

Fig. 10(b) displays the waveforms of the inverter voltage and current for  $V_{dc} = 400 \text{ V}$  and  $V_{bat} = 440 \text{ V}$ . Given that  $\sqrt{L_r/L_1}/(k_{lim}c_1c_2) = 1.03$  and  $V_{bat}/V_{dc} = 1.10$ , the ZVS condition (36) is not satisfied. The simulation waveforms demonstrate a failure in ZVS turn-on due to the inverter current being negative as the inverter voltage transitions from positive to negative.

#### E. OUTPUT POWER CHARACTERISTICS WITH INPUT AND OUTPUT VOLTAGES

An analysis of the output power characteristic concerning both input and output voltages has been conducted. This

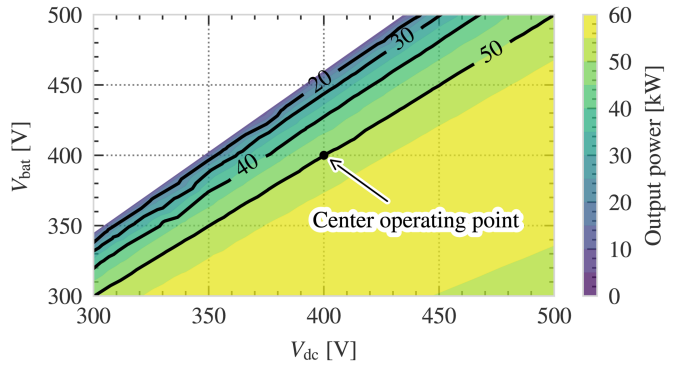


**FIGURE 11.** Output power characteristic with the input and output voltages.

analysis employs the theoretical equations (30) and (32) to determine the behavior of the system. The outcome of this analysis is visually illustrated in Fig. 11. The designed system delivers 50 kW when  $V_{dc} = V_{bat} = 400 \text{ V}$ , corresponding to the central operating point. To operate under light load conditions, two key approaches can be considered; decreasing the input voltage  $V_{dc}$  or increasing the output voltage  $V_{bat}$ . To achieve decreasing input voltage  $V_{dc}$ , reducing the inverter's switching phase or duty can be utilized. By decreasing effective  $V_{dc}$  in this manner, the system's power output can match the reduced load requirements. Alternatively, if the inverter controller cannot observe the load demands but the vehicle side needs to be operated at light load conditions, increasing the output voltage  $V_{bat}$  can be used. This can be accomplished by incorporating a dc-dc converter at the output port of the system. The dc-dc converter can step up the voltage level, allowing the system to maintain the output power at light loads. These strategies provide flexibility in adapting the system's performance to varying load conditions, providing efficient operation across a wide range of power requirements, from full load to light load.

#### F. SENSITIVITY ANALYSIS

In a real-world experimental setup, production errors associated with resonant capacitors and the presence of other parasitic components result in discrepancies between the actual and the ideally designed circuit parameters. Since the proposed circuit adds multiple resonant capacitors in the compensation network, the system characteristic would exhibit higher sensitivity compared to the conventional reflexive tuning circuit. To address this concern, a sensitivity analysis of all compensation components is conducted by sweeping the variation of each component from 90% to 110%.

The analysis results of the transmitter side and receiver side are shown in Fig. 12(a) and (b), respectively. The sensitivities of output power and uncoupled transmitter current are shown in the graphs. The impacts of the additional capacitors  $C_{1,\text{add}}$  and  $C_{r,\text{add}}$  on the system are relatively minor when compared to those of the other capacitors. Conversely, variations in  $C_{1,s}$  and  $C_{r,s}$  significantly affect the characteristics of the output

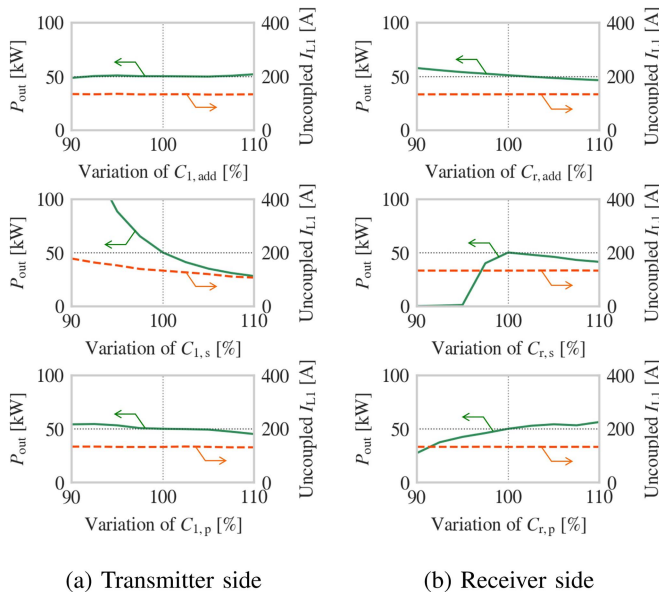


**FIGURE 12.** LTspice-simulated sensitivity analysis results with respect to compensation components.

power  $P_{\text{out}}$ . The increase in the output power leads to an increase in the current and voltage of the transmitting and receiving coils, thereby necessitating particular attention to errors in  $C_{1,s}$  and  $C_{r,s}$ . Additionally, reducing errors in  $C_{1,s}$  is beneficial to prevent unbalance in the uncoupled transmitter currents  $I_{L1}$ . To solve the variation issue of  $C_{1,s}$  and  $C_{r,s}$ , multi-series parallel configuration of capacitor components can be utilized. Instead of using a single capacitor with a current capacity  $I$  and voltage rating  $V$ , using capacitors with a current capacity of  $I/n$  ( $n$ : Natural number) and a voltage rating of  $V/n$  in  $n$  series and  $n$  parallel configurations can average out the production errors of capacitors. As a result, the total capacitance of the capacitors remains the same, but the total capacitance error can be reduced to  $1/n$ . Due to the trade-off between the increase in the number of components and the increase in component size for error reduction, it is necessary to find the minimum number of series-parallel combinations,  $n$ , that satisfies the acceptable error range of the total capacitance.

## V. EXPERIMENTAL VALIDATION

The proposed reflexive tuning DIPT system delivering 50-kW was constructed based on the presented design to verify the validity of the proposed circuit.

### A. COIL PROTOTYPE

The dimensions of the transmitter and receiver coils are shown in Fig. 13. The coils were constructed with an 8000-strand Litz wire with a strand diameter of 0.1 mm. The outer diameter of the wire, including the insulation, is 16.4 mm. The air gap between the transmitter and receiver coils is set at 223 mm. MnZn ferrite core (PC95, TDK) with 5 mm

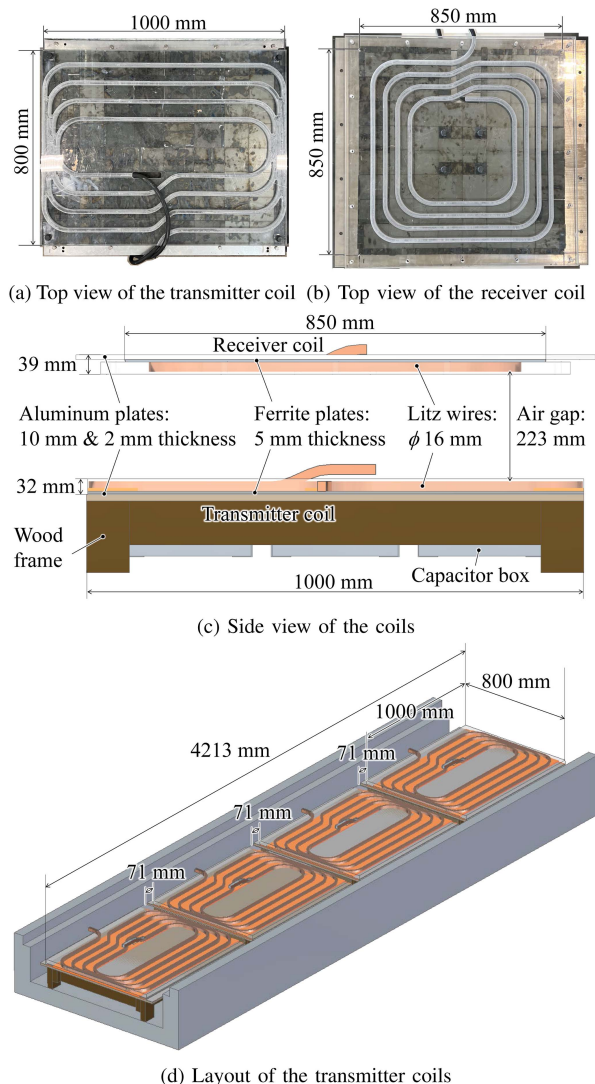


**FIGURE 13.** Detail of the prototype coils.

thickness is used for wireless coils. Fig. 13(a) shows the dimensions of the transmitter coils. The aluminum backplate used for shielding is placed in the bottom layer, the ferrite plate is placed in the middle layer, and the transmitter coil embedded in a coil former is placed on the top layer. Fig. 13(b) shows the dimension of the receiver coil. The whole structure is similar to the transmitter coil. Fig. 13(c) shows the dimension of the thickness of the prototype system. Coil formers are made of transparent acrylic sheets, and the Litz wires are embedded. Fig. 13(d) shows the layout of the transmitter coils. Each transmitter coil has a gap of 71 mm. Hence, the total length of the four transmitter coils is 4213 mm.

### B. 50 KW TEST RESULTS

The constructed 50 kW prototype system on an automated rail setup is shown in Fig. 14. The receiver coil is set on the cart, and an electric motor drives the cart at a constant speed with a maximum speed of 10 km/h.

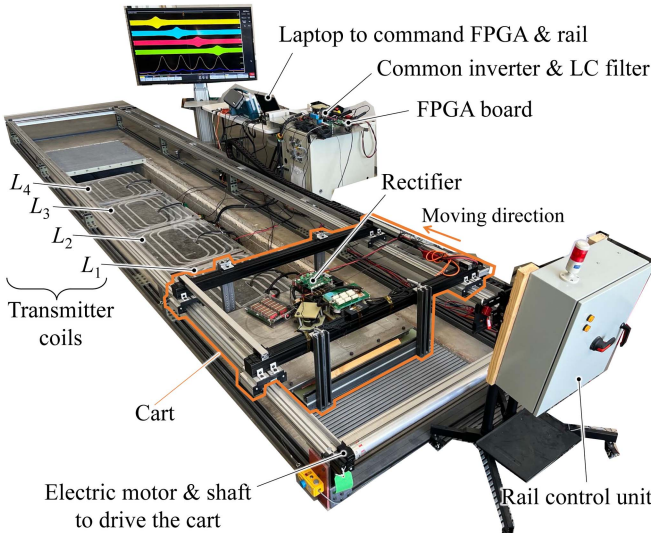


**FIGURE 14.** Overview of the automated rail setup.

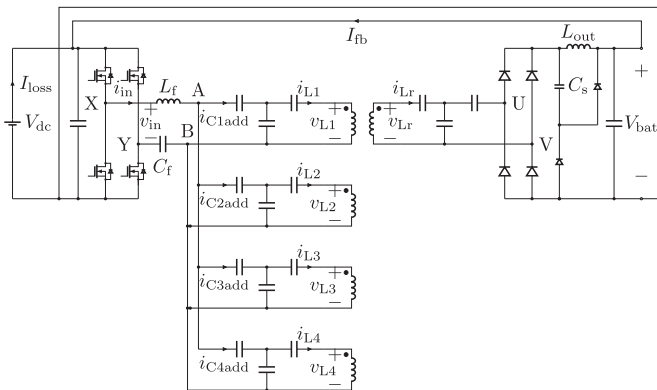


**FIGURE 15.** Circuit diagram of the experiment in the rail setup.

The circuit diagram of the experimental setup with energy feedback for power loss and efficiency measurements is shown in Fig. 15. Both the input and output voltages are fixed at 400 V. The power feedback via a dc wire allows the circulating of the transferred power within the system instead of dissipating the energy in a resistive load. While the transferred power is circulated, total losses are drawn from the external dc supply. Hence, the total power loss can be determined by measuring the dc current  $I_{\text{loss}}$  and the dc supply voltage  $V_{\text{dc}}$ . The transferred power can be calculated from the measured feedback current  $I_{\text{fb}}$  and the dc output voltage  $V_{\text{bat}}$ . Considering the high switching frequency of 85 kHz, silicon carbide (SiC) half-bridge MOSFETs module (CAS325M12HM2) with a rating voltage of 1.2 kV are used to minimize switching losses. A passive lossless snubber [39] is implemented in the output dc inductor  $L_{\text{out}}$  to mitigate the voltage spike created in the current-type rectifier. The same SiC MOSFET modules are used as the diode rectifier and

**TABLE 4.** System Parameters of the Experimental Setup

Parameter	Symbol	Value	Unit
Input voltage	$V_{\text{dc}}$	400	V
Output voltage	$V_{\text{bat}}$	400	V
Air gap	$z_{\text{gap}}$	223	mm
Switching frequency	$f_{\text{sw}}$	85	kHz
Coupling coefficient between $L_1$ & $L_r$	$k_{1,r}$	0.00~0.22	-
Limit of $k_{1,r}$	$k_{\text{lim}}$	0.23	-
Transmitter coil inductance	$L_1$	24.62	$\mu\text{H}$
Receiver coil inductance	$L_r$	23.19	$\mu\text{H}$
Filter inductor	$L_f$	5.31	$\mu\text{H}$
Filter capacitor	$C_f$	0.66	$\mu\text{F}$
Output dc inductor	$L_{\text{out}}$	15.00	$\mu\text{H}$
Output dc capacitor	$C_{\text{out}}$	10.00	$\mu\text{F}$
Snubber capacitor	$C_s$	0.1	$\mu\text{F}$
Transmitter coil's turn number	$N_{L1}$	4	turn
Receiver coil's turn number	$N_{Lr}$	4	turn
Added series capacitor	$C_{1,\text{add}}$	2.12	$\mu\text{F}$
Series capacitor	$C_{1,s}$	220	nF
Parallel capacitor	$C_{1,p}$	450	nF
Series capacitor	$C_{r,\text{add}}$	660	nF
Added series capacitor	$C_{r,s}$	238	nF
Parallel capacitor	$C_{r,p}$	484	nF
Ratio of capacitors $1 + C_{1,p}/C_{1,\text{add}}$	$c_1$	1.21	-
Ratio of capacitors $1 + C_{r,p}/C_{r,s}$	$c_2$	3.04	-
Ratio of capacitors $1 + C_{r,p}/C_{r,\text{add}}$	$c_3$	1.73	-

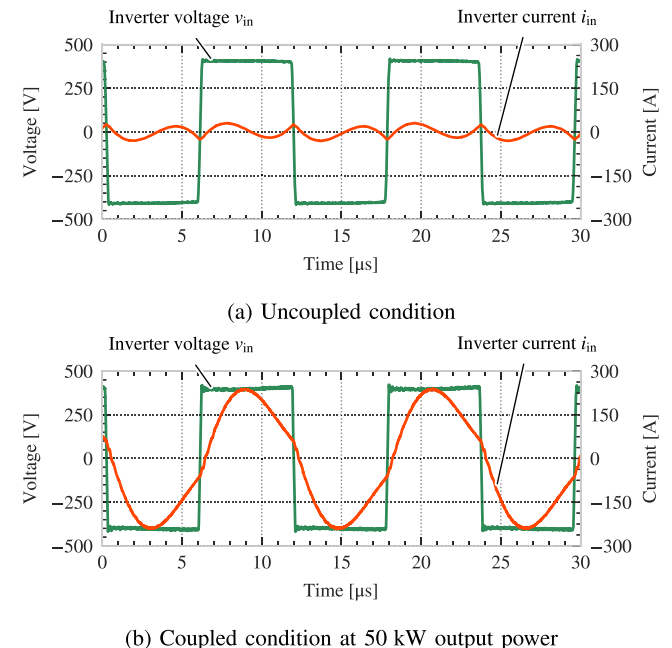


**FIGURE 16.** Experimental waveforms of the inverter voltage  $v_{\text{in}}$  and inverter current  $i_{\text{in}}$ .

snubber diodes. The values of each circuit component are listed in Table 4.

Waveforms of the inverter voltage  $v_{\text{in}}$  and the inverter current  $i_{\text{in}}$  in the uncoupled and coupled conditions are shown in Fig. 16. In the uncoupled condition, the inverter current amplitude of the switching frequency is close to zero, and there is only the harmonic component, as shown in Fig. 16(a). In the coupled condition, the inverter current  $i_{\text{in}}$  increases with sinusoidal waveform, maintaining the lagged current relative

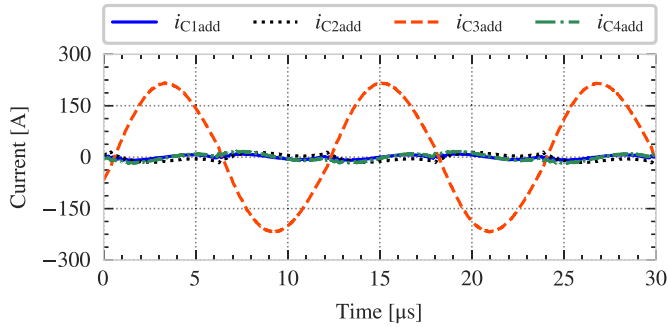


**FIGURE 17.** Series capacitor currents  $i_{C1add}$ ,  $i_{C2add}$ ,  $i_{C3add}$ , and  $i_{C4add}$  when the transmitter coil  $L_3$  is active at 50 kW output power.

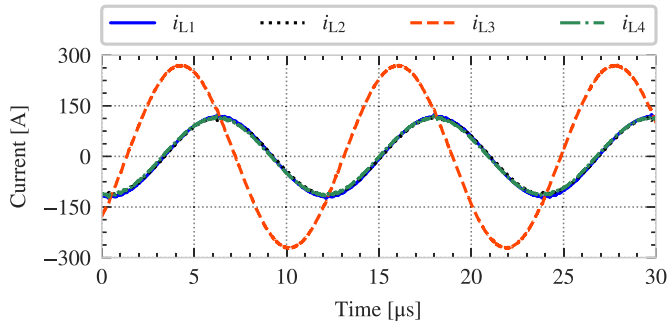


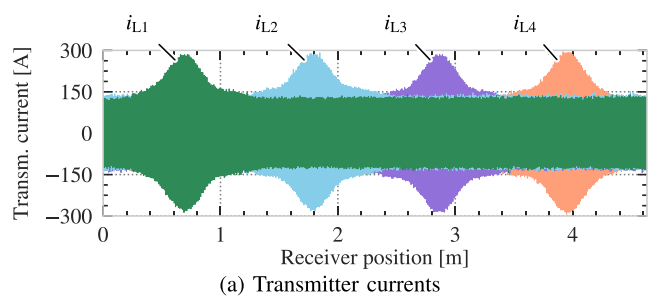
**FIGURE 18.** Transmitter coil currents  $i_{L1}$ ,  $i_{L2}$ ,  $i_{L3}$ , and  $i_{L4}$  when the transmitter coil  $L_3$  is active at 50 kW output power.

to the inverter voltage  $v_{in}$  for ZVS requirement, as shown in Fig. 16(b). The measured amplitude of the inverter current  $i_{in}$  is 238 A, and the output power is 50 kW in the coupled condition.

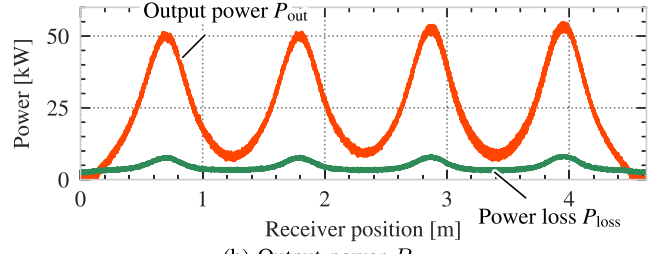
The current waveforms in the series capacitors  $C_{1,add}$ ,  $C_{2,add}$ ,  $C_{3,add}$ , and  $C_{4,add}$  when the third transmitter coil  $L_3$  is coupled are shown in Fig. 17. The current amplitudes of all the series capacitors in the uncoupled transmitters are close to zero. The measured amplitude of the series capacitor current  $i_{C3add}$  is 215 A.

The current waveforms of transmitter coils  $L_1$ ,  $L_2$ ,  $L_3$ , and  $L_4$  when the third transmitter coil  $L_3$  is coupled with the receiver coil  $L_r$  are shown in Fig. 18. The current amplitudes of all the uncoupled transmitters are 120 A. Only the coupled transmitter coil current  $i_{L3}$  is amplified to 270 A. The voltage of the transmitter coil  $v_{L3}$  is amplified from 1500 V in the uncoupled condition to 2590 V in the coupled condition. In the coupled condition, sinusoidal voltage and current are induced in the receiver coil. The amplitude of the receiver coil voltage is 3670 V, and the current is 363 A at 50 kW output power.

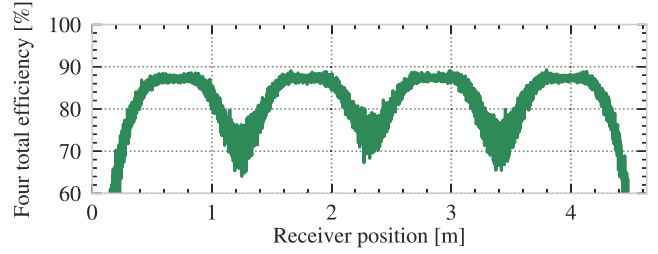
The stray magnetic fields from the uncoupled transmitter coils are measured at 800 mm away from the center of the uncoupled transmitter coil, and the measurement height is 110 mm from the top surface of the transmitter coil. The measured stray fields are compared to the SAE static wireless charging standard value [37]. The standards for where or how



(a) Transmitter currents



(b) Output power  $P_{out}$



(c) System dc-dc efficiency including four transmitter coils

**FIGURE 19.** Distribution of transmitter currents, output power, and efficiency at 10 km/h.

to measure stray fields for DIPT applications are still in development. In the recently published technical information report for J2954/2 for heavy-duty electric vehicles, an appendix is included for DIPT applications that suggest fields in dynamic systems will be measured at the edge of the lane rather than the edge of the vehicle when vehicles are traveling at speeds above 10 km/h [40]. At lower speeds, the requirement reverts to that of static wireless charging systems and could be achieved in DIPT systems with the proposed solution by disabling or reducing the currents when vehicles are operated at low speeds. Thus, measuring 800 mm from the side of a dynamic charging system is expected to be acceptable for roadway applications. In the uncoupled condition, the measured stray field is 23.9  $\mu$ T(rms), below the SAE stationary charging standard value of 27.0  $\mu$ T(rms).

The receiver coil is moved above the transmitter coils from edge to edge of the system at a constant speed of 10 km/h. The distributions of transmitter currents, output power, power loss, and efficiency are measured, as shown in Fig. 19. The measured transmitter currents with respect to the receiver coil position are shown in Fig. 19(a). The amplitudes of the transmitter coils naturally increase only when the receiver coil passes above each transmitter coil. The measured output power and power loss with respect to the receiver coil position

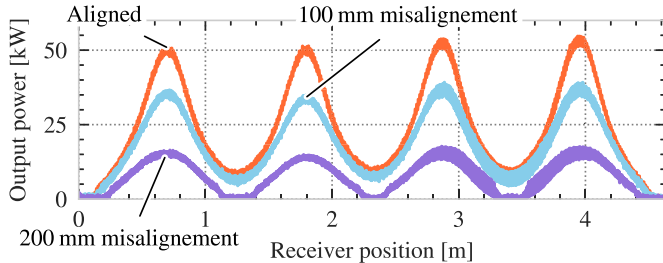


**FIGURE 20.** Comparison between the aligned and misaligned conditions.

are shown in Fig. 19(b). The output power distribution has peaks of 50 kW when the receiver coil is above the centers of each transmitter coil. The average output power is 25.1 kW. The minimum output power in the edge of transmitter coils is 9.2 kW with the least coupled condition. A longer transmitter coil might mitigate the effect of the edge dip of the output power since the main power output area depends on the center of the transmitter coil, and the edge dip effect on the average output power becomes almost negligible. Moreover, the combination of DD transmitter coils and a DDQ receiver coil [11] might solve the edge dip of the output power since the combination smooths the coupling profile over the car's driving direction. This research uses the circular coil for both the transmitter and receiver coils to verify the pure characteristics of the proposed reflexive tuning circuit in simplified conditions.

The efficiency distribution calculated from the measured output power and power loss is shown in Fig. 19(c). The dc-dc efficiency, including four transmitter coils, is 87.9% at 51.7 kW when the receiver coil is centered above the third transmitter coil  $L_3$ .

Output power distributions with 100 mm and 200 mm misalignments in the lateral direction are shown in Fig. 20. The peak power in the 100 mm misalignment condition is decreased by 30% compared to the aligned condition. The peak power in the 200 mm misalignment condition is decreased by 70% compared to the aligned state. The misalignment tolerance can be improved if the transmitter coil width is enlarged.

The power loss of each component of the proposed reflexive and the double-sided LCC circuits in the aligned condition can be estimated using the theoretical equations, as shown in Fig. 21. In the estimations, the first transmitter  $L_1$  is activated, and output power is 50 kW. The quality factors of all coils and capacitors  $Q_L$  and  $Q_C$  included in the system are defined as

$$Q_L = \frac{\omega L}{r_L} = 400 \quad (38)$$

$$Q_C = \frac{1}{\omega C r_C} = 500 \quad (39)$$

where  $r_L$  and  $r_C$  represent the equivalent series resistance of  $L$  and  $C$ , respectively. As shown in Fig. 21(a), the estimated total power loss of the proposed reflexive tuning is 6720 W, and the estimated total dc-dc efficiency with the

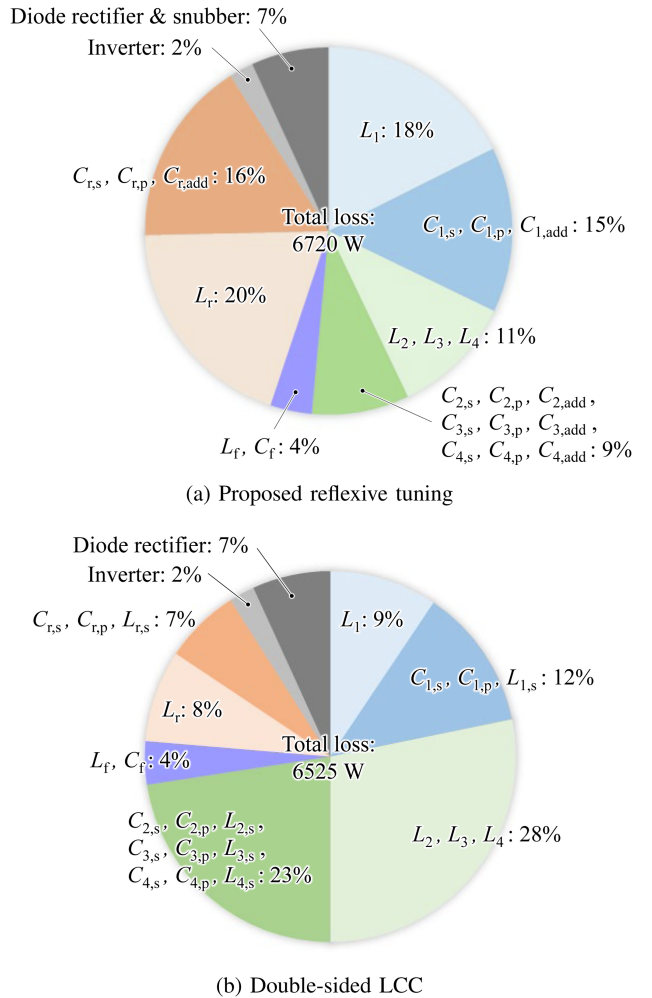


**FIGURE 21.** Estimated loss breakdown with four transmitter configurations when the output power is 50 kW.

four transmitter configurations is 88.2%, which is close to the measured dc-dc efficiency of 87.9%. The main loss factors are the coupled transmitter coil  $L_1$  and the receiver coil  $L_r$ . The loss of the uncoupled transmitter coils and their compensation components are maintained at a low level since the uncoupled transmitters have 2.25 times lower currents than the coupled transmitter. For a comprehensive understanding, an estimated loss breakdown of the conventional double-sided LCC circuit with four transmitter configurations is shown in Fig. 21(b).  $L_{1,s}$ ,  $L_{2,s}$ ,  $L_{3,s}$ ,  $L_{4,s}$ , and  $L_{r,s}$  represent series inductors in the conventional double-sided LCC circuit. Other notations of the circuit parameters are the same as the proposed reflexive tuning circuit. Due to the constant transmitter current characteristic of the double-sided LCC circuit, the loss from the uncoupled transmitter coils represents the highest percentage, accounting for 28% of the system's total loss.

The comparison between the theoretical and experimental total dc-dc efficiencies of the proposed circuit is listed in Table 5. The experimental efficiency with the single and the four transmitter coils are 90.0% and 87.9%, respectively. The

**TABLE 5.** Comparison of the Theoretical and Experimental Total dc-dc Efficiencies of the Proposed Circuit

Configuration	Theoretical efficiency	Experimental efficiency
Single transmitter coil	90.2%	90.0%
Four transmitter coils	88.2%	87.9%

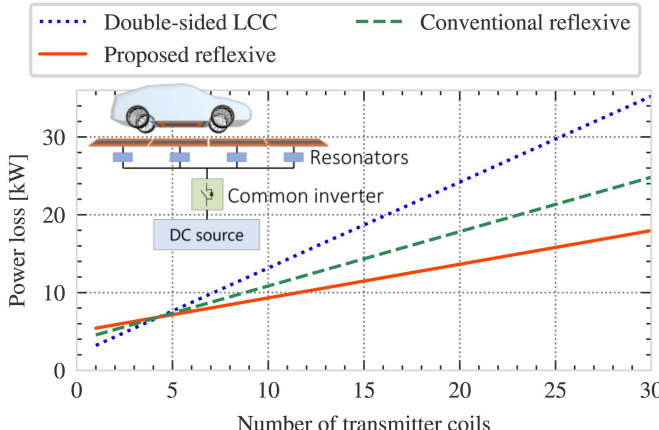


**FIGURE 22.** Theoretical power loss versus number of transmitters with 50 kW design.

experimental total dc-dc efficiency with the four transmitter configurations is directly measured from the experimental setup, and the value matches the theoretical model's efficiency within 0.3% error. The experimental efficiency with the single transmitter configuration is calculated using the measured loss of the four transmitter configurations and the theoretical loss difference between the single and four transmitter coils configurations.

Utilizing the theoretical loss model, how power loss varies with the number of parallel connected transmitters of 50 kW design are compared among the double-sided LCC circuit [33], conventional reflexive tuning circuit [34], and the proposed reflexive tuning circuit, as depicted in Fig. 22. All the circuit topologies assume parallel connected transmitters and compensation networks with a single inverter. The system design of output power is 50 kW. The dotted line represents the power loss of the double-sided LCC circuit. As the number of paralleled transmitters increases, its power loss grows significantly due to the constant current in each transmitter coil.

The dashed line shows the power loss of the conventional reflexive tuning circuit. For configurations with more than four parallel transmitters, this circuit exhibits reduced power loss compared to the double-sided LCC configurations, primarily due to the reduction in transmitter current in uncoupled transmitters.

The solid line illustrates the power loss of the proposed reflexive tuning circuit. For up to four parallel configurations, its power loss is higher than both the double-sided LCC and conventional reflexive tuning circuits, owing to additional components. However, for more than four parallel transmitter

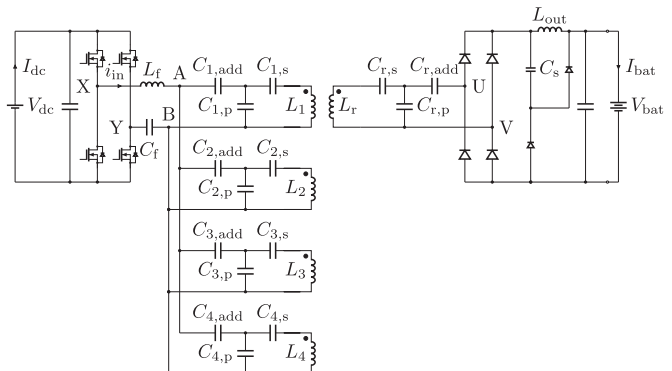


**FIGURE 23.** Schematic diagram of the vehicle test setup.

configurations, its power loss is less than that of the other two circuits. This is attributed to the substantially lower uncoupled transmitter currents in the proposed circuit compared to the double-sided LCC and conventional reflexive tuning circuit.

Therefore, the proposed circuit can achieve lower loss than the double-sided LCC and conventional reflexive tuning circuit if the transmitters are connected over four in parallel.

### C. 60 KM/H TEST RESULTS

The constructed rail setup cannot move the cart over the speed of 10 km/h. To evaluate the output power response over the maximum speed, and the validity of the proposed circuit in an actual application, the proposed circuit is implemented in a vehicle system. The schematic diagram of the vehicle test setup is shown in Fig. 23. An auxiliary battery is implemented on an electric vehicle as an output-side battery. The input voltage is reduced from 400 V to 250 V to reduce the peak output power from 50 kW to 20 kW. The output voltage is set to 350 V since the battery's voltage range is 300 to 400 V, which is a practical range for electric vehicles. Due to the utility restriction in the depth of the trench, the air gap between the transmitter and receiver coils is changed from 223 mm to 170 mm. The series compensation capacitor  $C_{r,s}$  is changed from 238 nF to 357 nF to adjust the difference of the peak coupling coefficient between the transmitter and receiver coils.

The overview of the constructed vehicle system is shown in Fig. 24. The transmitter coils are implemented in a trench and covered with fiberglass lids, enabling vehicles to run over them. The common inverter and the LC filter are implemented in the shed. Only the two wires from the LC filter are wired through a hole between the shed and the outside trench. Junctions for nodes A and B are implemented in the outside trench, and each transmitter and compensation capacitor is connected to the nodes. In contrast to the conventional short-individual transmitter configuration, the common inverter configuration can reduce the number of wires between the inverter and transmitter coils as well as the number of the inverters.

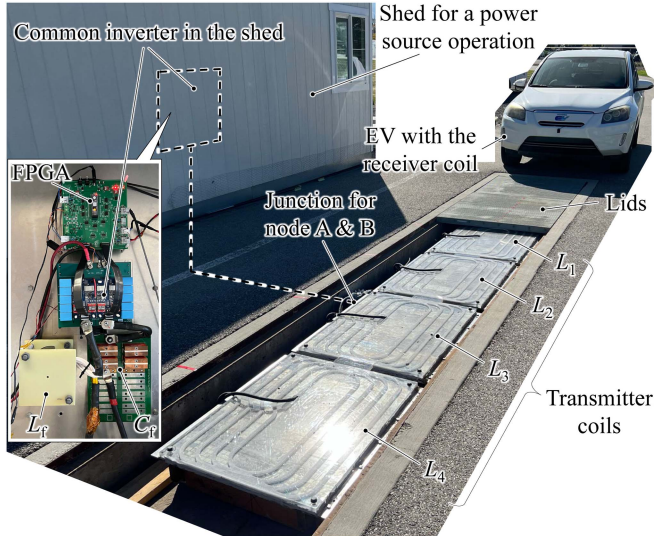


**FIGURE 24.** Overview of the vehicle test setup.

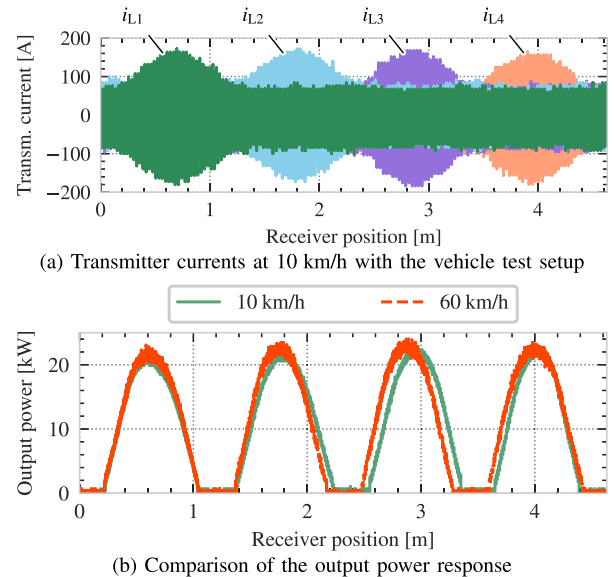


**FIGURE 26.** Distribution of transmitter currents and output power with the vehicle test setup.

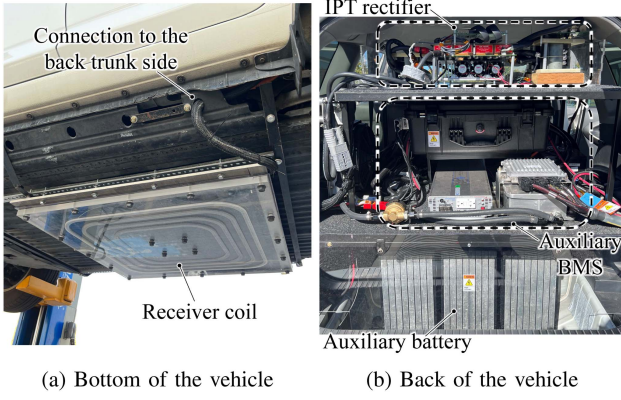


**FIGURE 25.** Overview of the experimental vehicle system.

The details of the vehicle system are shown in Fig. 25. Fig. 25(a) displays the receiver coil located underneath the vehicle. This coil is attached to the vehicle's bottom and linked to the IPT rectifier. Fig. 25(b) shows the vehicle's trunk. The rectifier's dc output is connected to the auxiliary battery through the auxiliary battery management system (BMS) box.

The transmitter current distributions when the vehicle runs at 10 km/h are shown in Fig. 26(a). The measured uncoupled and coupled transmitter current is 75 A and 165 A, respectively.

Fig. 26(b) presents the test results of the output response in case of two speeds: 10 km/h and 60 km/h, with the latter being the maximum speed limit of the test track. The output power distribution at the transmitter coils' edge differs from the rail test, as changes in the air gap alter the coupling coefficient distribution. While there's a difference in the timing of the third output power wave, attributed to challenges in maintaining a consistent vehicle speed, the overall shape of each output power waveform remains consistent between 10 km/h

and 60 km/h. Therefore, the results demonstrate the capability of power delivery at least up to 60 km/h with negligible time delay.

## VI. CONCLUSION

This paper has proposed a novel reflexive tuning circuit that leverages reflected reactance, enabling a single inverter to drive multiple transmitter coils. The simulation results demonstrate that the proposed circuit can reduce the uncoupled transmitter currents by 21% compared to the conventional reflexive tuning circuit and by 37% compared to the double-sided LCC circuit, all while maintaining the same output power level. The result of the soft switching analysis shows the ZVS condition of the proposed circuit is independent of the coupling coefficient between the transmitter and receiver coil. A 50 kW version of the proposed circuit with 223 mm air gap was built, achieving measured dc-dc efficiencies of 90.0% with a single transmitter coil configuration. Finally, the validity of the proposed circuit in high speed was demonstrated in the 60 km/h speed test using a vehicle.

## REFERENCES

- [1] B. J. Limb et al., "Economic viability and environmental impact of in-motion wireless power transfer," *IEEE Trans. Transp. Electrific.*, vol. 5, no. 1, pp. 135–146, Mar. 2019.
- [2] C. C. Mi, G. Buja, S. Y. Choi, and C. T. Rim, "Modern advances in wireless power transfer systems for roadway powered electric vehicles," *IEEE Trans. Ind. Electron.*, vol. 63, no. 10, pp. 6533–6545, Oct. 2016.
- [3] Z. Bi, T. Kan, C. C. Mi, Y. Zhang, Z. Zhao, and G. A. Keoleian, "A review of wireless power transfer for electric vehicles: Prospects to enhance sustainable mobility," *Appl. Energy*, vol. 179, pp. 413–425, 2016.
- [4] M. Budhia, G. A. Covic, and J. T. Boys, "Design and optimization of circular magnetic structures for lumped inductive power transfer systems," *IEEE Trans. Power Electron.*, vol. 26, no. 11, pp. 3096–3108, Nov. 2011.

- [5] G. A. Covic and J. T. Boys, "Inductive power transfer," *Proc. IEEE*, vol. 101, no. 6, pp. 1276–1289, Jun. 2013.
- [6] P. A. J. Lawton, F. J. Lin, and G. A. Covic, "Magnetic design considerations for high-power wireless charging systems," *IEEE Trans. Power Electron.*, vol. 37, no. 8, pp. 9972–9982, Aug. 2022.
- [7] K. W. Klontz, D. M. Divan, D. W. Novotny, and R. D. Lorenz, "Contactless power delivery system for mining applications," *IEEE Trans. Ind. Appl.*, vol. 31, no. 1, pp. 27–35, Jan./Feb. 1995.
- [8] W. Lee et al., "Finite-width magnetic mirror models of mono and dual coils for wireless electric vehicles," *IEEE Trans. Power Electron.*, vol. 28, no. 3, pp. 1413–1428, Mar. 2013.
- [9] S. Lee, B. Choi, and C. T. Rim, "Dynamics characterization of the inductive power transfer system for online electric vehicles by Laplace phasor transform," *IEEE Trans. Power Electron.*, vol. 28, no. 12, pp. 5902–5909, Dec. 2013.
- [10] S. Y. Choi, J. Huh, W. Y. Lee, and C. T. Rim, "Asymmetric coil sets for wireless stationary EV chargers with large lateral tolerance by dominant field analysis," *IEEE Trans. Power Electron.*, vol. 29, no. 12, pp. 6406–6420, Dec. 2014.
- [11] M. Budhia, J. T. Boys, G. A. Covic, and C.-Y. Huang, "Development of a single-sided flux magnetic coupler for electric vehicle IPT charging systems," *IEEE Trans. Ind. Electron.*, vol. 60, no. 1, pp. 318–328, Jan. 2013.
- [12] G. A. Covic, J. T. Boys, M. L. Kissin, and H. G. Lu, "A three-phase inductive power transfer system for roadway-powered vehicles," *IEEE Trans. Ind. Electron.*, vol. 54, no. 6, pp. 3370–3378, Dec. 2007.
- [13] C.-S. Wang, G. A. Covic, and O. H. Stielau, "Power transfer capability and bifurcation phenomena of loosely coupled inductive power transfer systems," *IEEE Trans. Ind. Electron.*, vol. 51, no. 1, pp. 148–157, Feb. 2004.
- [14] A. L. Stein, P. A. Kyaw, and C. R. Sullivan, "Wireless power transfer utilizing a high- $Q$  self-resonant structure," *IEEE Trans. Power Electron.*, vol. 34, no. 7, pp. 6722–6735, Jul. 2019.
- [15] L. Xue et al., "Modular power electronics approach for high power dynamic wireless charging system," *IEEE Trans. Transp. Electricif.*, vol. 10, no. 1, pp. 976–988, Mar. 2024.
- [16] H. Feng, R. Tavakoli, O. C. Onar, and Z. Pantic, "Advances in high-power wireless charging systems: Overview and design considerations," *IEEE Trans. Transp. Electricif.*, vol. 6, no. 3, pp. 886–919, Sep. 2020.
- [17] L. Chen, G. R. Nagendra, J. T. Boys, and G. A. Covic, "Double-coupled systems for IPT roadway applications," *IEEE J. Emerg. Sel. Topics Power Electron.*, vol. 3, no. 1, pp. 37–49, Mar. 2015.
- [18] D. Patil, M. K. McDonough, J. M. Miller, B. Fahimi, and P. T. Balsara, "Wireless power transfer for vehicular applications: Overview and challenges," *IEEE Trans. Transp. Electricif.*, vol. 4, no. 1, pp. 3–37, Mar. 2018.
- [19] C.-S. Wang, O. H. Stielau, and G. A. Covic, "Design considerations for a contactless electric vehicle battery charger," *IEEE Trans. Ind. Electron.*, vol. 52, no. 5, pp. 1308–1314, Oct. 2005.
- [20] A. Dayerizadeh, H. Feng, and S. M. Lukic, "Dynamic wireless charging: Reflexive field containment using saturable inductors," *IEEE Trans. Ind. Appl.*, vol. 56, no. 2, pp. 1784–1792, Mar./Apr. 2020.
- [21] J. Huh, S. W. Lee, W. Y. Lee, G. H. Cho, and C. T. Rim, "Narrow-width inductive power transfer system for online electrical vehicles," *IEEE Trans. Power Electron.*, vol. 26, no. 12, pp. 3666–3679, Dec. 2011.
- [22] S. Y. Choi, S. Y. Jeong, B. W. Gu, G. C. Lim, and C. T. Rim, "Ultraslim S-type power supply rails for roadway-powered electric vehicles," *IEEE Trans. Power Electron.*, vol. 30, no. 11, pp. 6456–6468, Nov. 2015.
- [23] G. A. J. Elliott, J. T. Boys, and G. A. Covic, "A design methodology for flat pick-up ICPT systems," in *Proc. IEEE 1st Conf. Ind. Electron. Appl.*, 2006, pp. 1–7.
- [24] B.-M. Song, R. Kratz, and S. Gurrol, "Contactless inductive power pickup system for maglev applications," in *Proc. IEEE Conf. Rec. Ind. Appl. Conf. 37th IAS Annu. Meeting*, 2002, vol. 3, pp. 1586–1591.
- [25] J. Huh, W. Lee, G.-H. Cho, B. Lee, and C.-T. Rim, "Characterization of novel inductive power transfer systems for on-line electric vehicles," in *Proc. IEEE 26th Annu. Appl. Power Electron. Conf. Expo.*, 2011, pp. 1975–1979.
- [26] G. A. Covic and J. T. Boys, "Modern trends in inductive power transfer for transportation applications," *IEEE J. Emerg. Sel. Topics Power Electron.*, vol. 1, no. 1, pp. 28–41, Mar. 2013.
- [27] S. Li and C. C. Mi, "Wireless power transfer for electric vehicle applications," *IEEE J. Emerg. Sel. Topics Power Electron.*, vol. 3, no. 1, pp. 4–17, Mar. 2015.
- [28] S. Zhou and C. C. Mi, "Multi-paralleled LCC reactive power compensation networks and their tuning method for electric vehicle dynamic wireless charging," *IEEE Trans. Ind. Electron.*, vol. 63, no. 10, pp. 6546–6556, Oct. 2016.
- [29] V. Cirimele, M. Diana, F. Freschi, and M. Mitolo, "Inductive power transfer for automotive applications: State-of-the-art and future trends," *IEEE Trans. Ind. Appl.*, vol. 54, no. 5, pp. 4069–4079, Sep./Oct. 2018.
- [30] J. M. Miller et al., "Demonstrating dynamic wireless charging of an electric vehicle: The benefit of electrochemical capacitor smoothing," *IEEE Power Electron. Mag.*, vol. 1, no. 1, pp. 12–24, Mar. 2014.
- [31] A. N. Azad, A. Echols, V. A. Kulyukin, R. Zane, and Z. Pantic, "Analysis, optimization, and demonstration of a vehicular detection system intended for dynamic wireless charging applications," *IEEE Trans. Transp. Electricif.*, vol. 5, no. 1, pp. 147–161, Mar. 2019.
- [32] V. Z. Barsari, D. J. Thrimawithana, and G. A. Covic, "An inductive coupler array for in-motion wireless charging of electric vehicles," *IEEE Trans. Power Electron.*, vol. 36, no. 9, pp. 9854–9863, Sep. 2021.
- [33] F. Lu, H. Zhang, H. Hofmann, and C. C. Mi, "A dynamic charging system with reduced output power pulsation for electric vehicles," *IEEE Trans. Ind. Electron.*, vol. 63, no. 10, pp. 6580–6590, Oct. 2016.
- [34] K. Lee, Z. Pantic, and S. M. Lukic, "Reflexive field containment in dynamic inductive power transfer systems," *IEEE Trans. Power Electron.*, vol. 29, no. 9, pp. 4592–4602, Sep. 2014.
- [35] R. Tavakoli and Z. Pantic, "Analysis, design, and demonstration of a 25-kW dynamic wireless charging system for roadway electric vehicles," *IEEE Trans. Emerg. Sel. Topics Power Electron.*, vol. 6, no. 3, pp. 1378–1393, Sep. 2018.
- [36] Z. Zhou, L. Zhang, Z. Liu, Q. Chen, R. Long, and H. Su, "Model predictive control for the receiving-side DC–DC converter of dynamic wireless power transfer," *IEEE Trans. Power Electron.*, vol. 35, no. 9, pp. 8985–8997, Sep. 2020.
- [37] *Wireless Power Transfer for Light-Duty Plug-in/Electric Vehicles and Alignment Methodology*, SAE J2954, Warrendale, PA, USA, 2019.
- [38] S. Inoue et al., "Fast design optimization method utilizing a combination of artificial neural networks and genetic algorithms for dynamic inductive power transfer systems," *IEEE Open J. Power Electron.*, vol. 3, pp. 915–929, 2022.
- [39] J.-G. Cho, J.-W. Baek, C.-Y. Jeong, and G.-H. Rim, "Novel zero-voltage and zero-current-switching full-bridge PWM converter using a simple auxiliary circuit," *IEEE Trans. Ind. Appl.*, vol. 35, no. 1, pp. 15–20, Jan./Feb. 1999.
- [40] S. International, "SAE TIR J2954/2: Wireless power transfer and alignment for heavy duty applications," *SAE Int. Tech. Inf. Rep. J2954/2\_202212*, 2022. [Online]. Available: [https://www.sae.org/standards/content/j2954/2\\_202212/](https://www.sae.org/standards/content/j2954/2_202212/)



**SHUNTARO INOUYE** (Member, IEEE) received the B.S. degree in mechanical, materials, and manufacturing science from Osaka University, Suita, Japan, in 2011, the M.S. degree in precision engineering from the University of Tokyo, Tokyo, Japan, in 2013, and the Ph.D. degree in electrical engineering from Utah State University, Logan, UT, USA, in 2023. In 2013, he joined Toyota Central R & D Labs., Inc., Nagakute, Japan, and was involved with a development team for high-power density dc–dc converters for next-generation hybrid vehicles. He has coauthored more than 15 peer-reviewed publications and has more than ten issued patents. His research interests include power electronics for electric vehicles and their infrastructures, including wireless power transfer systems, and high-power-density dc–dc converters. In 2019, he was the recipient of a Scholarship from Toyota Central R & D Labs., Inc. He was the recipient of the Japan Society of Mechanical Engineers Kansai-Branch Best Presentation Award in 2011, Institute of Electrical Engineers of Japan (IEEJ) Best Presentation Award in 2016, IEEJ Encouraging Prize Award in 2017, Outstanding Presentation Award in the 2019 IEEE APEC, IEEJ Distinguished Paper Award in 2020, and IEEJ Technical Development Award in 2021.



**SAMUEL KIGUTHI** is currently working toward the undergraduate degree in computer engineering with Utah State University (USU), Logan, UT, USA. He will graduate in 2024, and subsequently begin the master's degree in computer engineering during Fall 2024 with USU. He was an undergraduate Research Assistant with the Advancing Sustainability through Powered Infrastructure for Roadway Electrification (ASPIRE) Engineering Research Center, USU, and will conduct research as a part of the National Science Foundation Research Experiences for Undergraduate (NSF REU) with the Center for Extreme Ultraviolet Science and Technology (EUV ERC).



**JONATHAN NEWMAN** is currently working toward the B.S. degree in electrical engineering with Utah State University, Logan, UT, USA, and will graduate in 2024. He plans to work toward the M.S. degree in electrical engineering with Utah State University. In 2022, he became a research assistant with the Advancing Sustainability through Powered Infrastructure for Roadway Electrification (ASPIRE), where he assisted in the research and development of WPT systems for electric vehicles.



**TIMOTHY GOODALE** is currently working toward the B.S. degree in computer engineering with Utah State University (USU), Logan, UT, USA, and will graduate in 2024. He was a Research Assistant with Advancing Sustainability through Powered Infrastructure for Roadway Electrification (ASPIRE) with USU. He is also a Research Assistant with the USU Bridge Lab working under Dr. Chakraborty on AI hardware accelerators. He will be an intern this summer with Crane Aerospace and Electronics in Lynnwood, WA, USA and working on DC-DC converters for satellites.



**CHAKRIDHAR REDDY TEENETI** (Member, IEEE) received the B.Tech. degree in electrical engineering from Jawaharlal Nehru Technological University Hyderabad, Hyderabad, India, in 2013, the M.Tech. degree in electrical engineering from the Indian Institute of Technology Bombay, Mumbai, India, in 2015, and the Ph.D. degree in electrical engineering from Utah State University, Logan, UT, USA, in 2022. From 2015 to 2017, he was a Researcher with Hitachi India R & D, Bengaluru on uninterrupted power supplies.

Since 2022, he has held the position of Senior Engineer in Power Electronics Hardware with Lucid Motors. His research interests include transportation electrification, power conversion topologies and control methods, and static and dynamic wireless charging.



**BRYCE HESTERMAN** (Life Member, IEEE) received the B.S.E.E. and M.S.E.E. degrees from Brigham Young University, Provo, UT, USA, in 1987 and 1993, respectively. He is currently a Principal Research Engineer with the ASPIRE Engineering Research Center, Utah State University, Logan, UT, where he provides advanced engineering support, oversight, and leadership on major research and development projects. His industry experience includes designing power electronics for a variety of applications such as in-space electric propulsion, power supplies used in the plasma thin film industry, and electronic lighting ballasts. He invented or co-invented several soft-switching and resonant power converter topologies used in energy-efficient products, and has been awarded 26 patents. He enjoys modeling and simulation as well as designing and building electronic devices. He has been a Vice Chair and Chair of IEEE PELS chapters and is currently an Advisor to the USU student PELS chapter.



**ABHILASH KAMINENI** (Member, IEEE) received the B.E. (Hons.) degree in electrical engineering and the Ph.D. degree in power electronics from The University of Auckland, Auckland, New Zealand, in 2012 and 2017, respectively. He joined the Power Electronics Laboratory, Utah State University, Logan, UT, USA, as a Postdoctoral Fellow and an Assistant Professor, in 2017 and 2019, respectively. His main research interests include wireless power transfer and resonant converters.



**REGAN ANDREW ZANE** (Senior Member, IEEE) received the Ph.D. degree in electrical engineering from the University of Colorado Boulder, Boulder, CO, USA. He was an Assistant and Associate Professor with the University of Colorado-Boulder, Colorado Power Electronics Center, and a Research Engineer with GE Global Research Center, Niskayuna, NY, USA. He is currently the David G. and Diann L. Sant Endowed Professor with the Department of Electrical and Computer Engineering, Utah State University, Logan, UT, USA, and the Director of the NSF Engineering Research Center for Advancing Sustainability through Powered Infrastructure for Roadway Electrification. He has coauthored more than 200 peer-reviewed publications and the textbook *Digital Control of High-Frequency Switched-Mode Power Converters* (Wiley, 2015), and has more than 30 issued patents. He has recent and ongoing research programs in power electronics for electric vehicle charging infrastructure, including extreme fast charging and static and dynamic wireless charging, battery management systems, dc microgrids, grid-tied and grid-interactive converters, and grid integration of energy storage and renewable energy. Dr. Zane was the recipient of the National Science Foundation CAREER Award in 2004, 2005 IEEE Microwave Best Paper Prize, 2007 and 2009 IEEE Power Electronics Society Transactions Prize Letter Awards, 2008 IEEE Power Electronics Society Richard M. Bass Outstanding Young Power Electronics Engineer Award, 2006 Inventor of the Year, 2006 Provost Faculty Achievement, 2008 John and Mercedes Peebles Innovation in Teaching, 2011 Holland Teaching Awards from the University of Colorado, and the 2021 University Researcher of the Year Award from Utah State University.